Robust and Tunable Ferroelectricity in Ba/Co Codoped $(K_{0.5}Na_{0.5})NbO_3$ Ceramics

Jiaxun Liu (刘佳讯)[1†], Jielin Zha(查节林)[1†], Yulong Yang(杨玉龙)[1], Xiaomei Lu(吕笑梅)[1,2*],
Xueli Hu(胡雪莉)[1], Shuo Yan(阎朔)[1], Zijing Wu(吴子敬)[1], and Fengzhen Huang(黄凤珍)[1,2*]

[1]*National Laboratory of Solid State Microstructures and School of Physics, Nanjing University, Nanjing 210093, China*
[2]*Collaborative Innovation Center of Advanced Microstructures, Nanjing University, Nanjing 210093, China*

The $0.98(K_{0.5}Na_{0.5})NbO_3$-$0.02Ba(Nb_{0.5}Co_{0.5})O_{3-\delta}$ ceramics with doped Ba^{2+} and Co^{2+} ions are fabricated, and the impacts of the thermal process are studied. Compared with the rapidly cooled (RC) sample, the slowly cooled (SC) sample possesses superior dielectric and ferroelectric properties, and an 11 K higher ferroelectric-paraelectric phase transition temperature, which can be attributed to the structural characteristics such as the grain size and the degree of anisotropy. Heat treatment can reversibly modulate the content of the oxygen vacancies, and in turn the ferroelectric hysteresis loops of the samples. Finally, robust and tunable ferroelectric property is achieved in SC samples with good structural integrity.

Potassium-sodium niobate $(K_{0.5}Na_{0.5})$ NbO_3 (KNN) based ceramics have gained widespread research attention in recent years due to their excellent piezoelectric and ferroelectric properties, as well as the absence of toxic element lead (Pb). Their outstanding electrical properties make them promising for significant applications in energy harvesting, energy storage, information storage, and photoelectric detection, etc. [1–6]

The electrical properties of KNN-based ceramic could be modulated by different methods such as texture sintering, chemical doping, domain engineering and compositing. [7,8] For example, Satio *et al.* prepared KNN-based textured ceramics using the reactive template grain growth method and achieved excellent piezoelectric properties. [9] Through domain engineering, Wang *et al.* improved the piezoelectric coefficient of the KNN-based ceramics to 324 pC/N. [10] Zhang *et al.* designed compositional gradient piezoelectric ceramics that exhibit superior temperature reliability. [11]

Among the modulation methods, doping is easy and has remarkable effects on the properties. [12,13] For instance, high piezoelectric voltage (5.6 V) was achieved through Li/Ta doping in the KNN ceramic fibers. [14] Dielectric relaxation behavior was induced in Li/Sb-doped KNN bulk materials. [3] Sb doping could modulate the long-range ferroelectric order, so as to construct the multiphase coexistence near room temperature, and result in a nearly twofold increase in piezoelectric coefficient $(d_{33} \sim 539 \text{ pC/N})$. [15] In Ni/Ba co-doped KNN ceramics, the ferroelectric domains and domain walls could be reversibly controlled through light illumination. [16]

Most of the doped cations possess the same valence with that of either A-site K/Na or B-site Nb ions. Because of the difference in ion radius, lattice distortion and domain reconfiguration could be induced, thereby altering the macroscopic properties of the ceramics. As we know, doping with elements of different valences might introduce oxygen vacancies that could have additional impacts on the physical properties. [17,18] It is reported that oxygen vacancies introduced by Mg^{2+}-doping significantly increase the dielectric constant of $BiFeO_3$. [4] The oxygen vacancies caused by doped rare earth elements Pr/Sm dominated the conductivity of KNN ceramics, leading to photoluminescence. [19] Min *et al.* further showed that heat treatment could modulate the content of oxygen vacancies, thereby regulating the dielectric and mechanical relaxation behavior of $BiFeO_3$ ceramics. [20] In general, fewer studies focused on heterovalent doping of KNN, and effect of doping on the electrical properties needs to be deeply revealed. [12,21]

In this study, we introduce Ba^{2+} and Co^{2+} ions at A and B sites, to replace the original K^+/Na^+ and Nb^{5+} ions, respectively. This heterovalent doping introduced additional oxygen vacancies, thus providing additional degrees of freedom for regulating ferroelectric properties. On this basis, we explore the effects of cooling rate after sintering on the microstructure and the macroscopic electrical properties of the KNN-based ceramics. We demonstrate that, compared with ceramics experiencing a rapid cooling process, the slowly cooled samples have more complete lattice structures, larger degree of anisotropy, as well as superior dielectric and ferroelectric properties. The heat treatments under different atmospheres could modulate the content of oxygen vacancies, and in turn the ferroelectric polarization switching.

Sample Preparation and Characterization. We introduced 2 mol% of $Ba(Nb_{0.5}Co_{0.5})O_{3-\delta}$ into potassium-sodium niobate, that is, doping A and B sites with Ba^{2+} and Co^{2+} respectively to fabricate the $0.98(K_{0.5}Na_{0.5})NbO_3$-$0.02Ba(Nb_{0.5}Co_{0.5})O_{3-\delta}$ ceramics.

[†]These authors contributed equally to this work.
[*]Corresponding authors. Email: xiaomeil@nju.edu.cn; fzhuang@nju.edu.cn

The ceramic samples were synthesized via the solid-state reaction method, from the starting reactants (Sinopharm Chemical Reagent Co., Ltd) of K_2CO_3 ($\geq$99.0%), Na_2CO_3 ($\geq$99.8%), $BaCO_3$ ($\geq$99.0%), Nb_2O_5 ($\geq$99.99%), and CoO ($\geq$99.0%). To ensure the stoichiometry, we dried the carbonates in an oven at 180 ℃ for 8 h before weighting. Reactants were weighted by exact stoichiometry and mixed in the clean agate jar with absolute ethyl alcohol. The mixing and milling procedure continued 24 h in a planetary ball mill machine. After the slurry being dried at 80 ℃ for 12 h and then ground for 0.5 h in the agate mortar, reactants were sieved by a 120-mesh sieve and transferred into an alumina crucible to calcine at 850 ℃ for 6 h in air. The above reaction products were milled, dried, and sieved again, then mixed with 5% polyvinyl alcohol solution (PVA) and pressed into circular green bodies at 200 MPa. The green bodies were heated to 550 ℃ for 3 h to remove the PVA and then sintered at 1165 ℃ for 2 h with a 5 ℃/min heating rate. Later for the cooling process, two different cooling rates were adopted: 0.5 ℃/min (slow cooling, abbreviated as SC) and 10 ℃/min (rapid cooling, abbreviated as RC). The sintered ceramics were reduced to 0.1–0.2 mm thickness, and on both sides, Pt layers were sputtered for electrical measurements with the top electrode about 2 mm in diameter.

An x-ray powder diffractometer (XRD, Bruker D8, Cu Kα), a scanning electron microscope (SEM, FEI Quanta200), a polarized light microscope (PLM, OLYMPUS BX53F2), and an x-ray photoelectron spectroscope (XPS, ULVACPHI PHI5000 Versa Probe) were used to characterize the microstructure of the samples. A standard ferroelectric test unit (TF-2000, aix-ACCT) and a computer-controlled precision LCR impedance analyzer (HP4294, Agilent) were employed to measure the hysteresis loops (100 Hz) and the dielectric spectrum (100 Hz–1 MHz, 25–430 ℃), respectively.
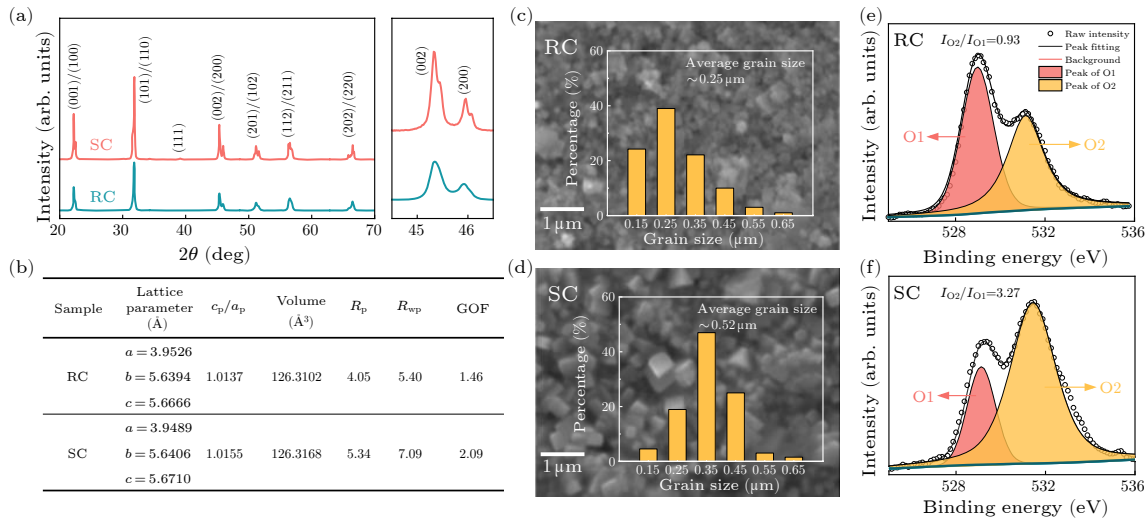
Fig. 1. (a) Room temperature XRD diffraction patterns of the RC and SC samples. (b) Parameters for Rietveld refinement. [(c), (d)] SEM images of the RC and SC samples. The insets are the corresponding statistics of grain size. [(e), (f)] XPS O 1s spectra of the samples.

Results and Discussion. The room-temperature XRD diffraction patterns [Fig. 1(a)] show that, both RC and SC samples are in polycrystalline orthorhombic structure, without any obvious impurity phases. It shows that the cooling rate has no obvious effect on the lattice structure of ceramic samples, which is consistent with literature.[1,3,14] However, the diffraction peaks of the SC sample are sharper than those of the RC sample, as seen more clearly from the local magnification in Fig. 1(a), which is often associated with the increase in grain size.

Structural refinement of the two samples was performed using the TOPAS software and $Amm2$ (ICSD#261355) space group, with the results given in Fig. 1(b) and Fig. S1 in the Supplementary Material. To compare with the high-temperature cubic phase, the unit cell parameters of the monoclinic phase are often used, written as $a_p = a$, $b_p = c_p = \sqrt{b^2 + c^2}/2$.[19] For the RC and SC samples, c_p/a_p are 1.0137 and 1.0155, respectively, indicating a higher degree of anisotropy for the SC sample.

Figures 1(c) and 1(d) show the SEM surface morphologies of the two samples, with the statistics of the grain size given in the insets. The grains in both the RC and SC samples exhibit hexahedral shapes of various sizes, showing the good crystallinity. Meanwhile, the average grain size of the SC sample is about 0.52 μm, obviously larger than that of the RC sample ($\sim$0.25 μm). The effect of cooling rate on grain size is easily understood: although the sintering temperature of the SC and RC samples are the same (1165 ℃), because of the slow cooling rate, the SC samples maintain in high temperatures longer, allowing more time for grain growth. Figure S2 gives the cross-sectional SEM images of the samples. The depressions in the images were formed by the detachment of grains during the breaking process, which means that the size of the depressions reflects the size of the grains inside the ceramics. It shows that the grain size inside the SC sample is also larger than that inside the RC sample, consistent with the observations on the surface [Figs. 1(c) and 1(d)]. Moreover, both the samples are very dense. In other words, although the cooling rate causes the difference in grain size, it has no observable

effect on the compactness of the ceramic samples.

In perovskite oxides, oxygen vacancies are common charged defects. As the original valent of the A and B site ions in KNN are +1 and +5 respectively, the introduction of Ba^{2+} at A site and Co^{2+} at B site would necessarily be accompanied by generation of oxygen vacancies. XPS testing was performed to estimate the content of oxygen vacancies in the samples. As shown in Figs. 1(e) and 1(f), the O 1s peak of the sample can be regarded as the superposition of two peaks: lattice oxygen O1 around 529.5 eV and adsorbed oxygen O2 around 531.3 eV. [22] The ratio of the integrated intensities of the two peaks I_{O2}/I_{O1} for the RC and SC samples are 0.93 and 3.27, respectively, indicating an obviously larger amount of oxygen vacancies in the SC sample. It shows that the RC process is beneficial for reducing the oxygen vacancies in KNN ceramics.

Figures S3 in the Supplementary Material shows the images of the RC and SC samples under a PLM at 0° and after being rotated 90°. Strips appear along specific directions [dashed rectangles in [Figs. S3(a) and S3(b)], and the light and the shade convert as the sample rotates [as indicated by the dashed circles in Figs. S3(a) and S3(c)], which could be attributed to the domain structures and their effect on the light transmission. The stripes in the SC sample are larger than those in the RC sample, indicating larger domain size, which is consistent with the larger grain size in the SC sample.
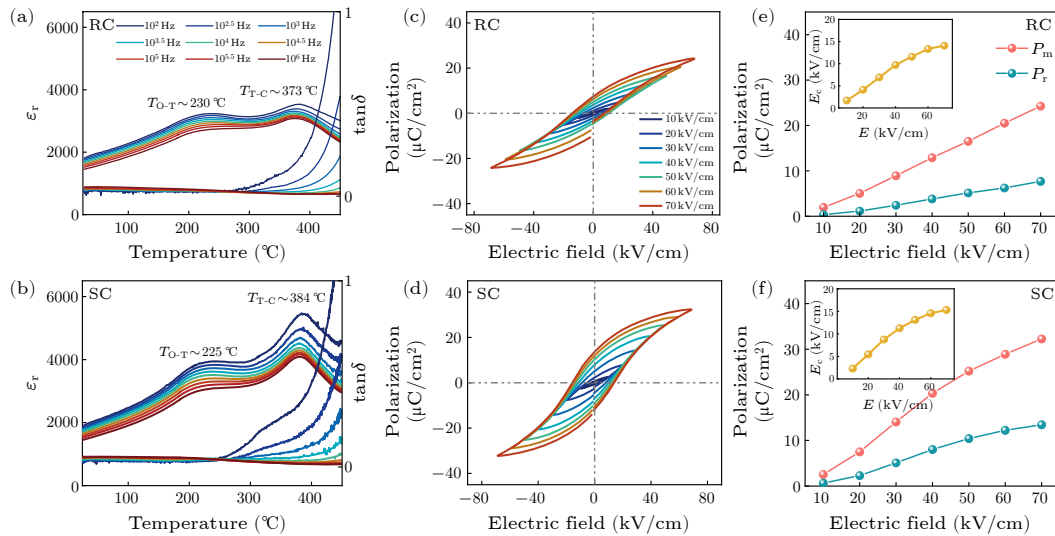
Fig. 2. [(a), (b)] Temperature dependent dielectric constant and dielectric loss of the RC and SC samples measured at different frequencies. [(c), (d)] Hysteresis loops of the RC and SC samples tested under different electric fields (100 Hz). [(e), (f)] Parameter changes corresponding to the hysteresis loops in (c) and (d).

Figures 2(a) and 2(b) show the dielectric spectra of the RC and SC samples in the temperature range of 25–450 ℃ and at different frequencies of 100 Hz–1 MHz. Both the samples exhibit two obvious dielectric peaks around 225–230 ℃ and 373–384 ℃, corresponding to the orthorhombic-tetragonal (O-T) phase transition and tetragonal-cubic (T-C) phase transition of KNN, respectively. [23] This means that, at room temperature, both the samples are in orthorhombic phase, consistent with the above XRD analysis. In addition, the dielectric loss is small, less than 0.06 in the temperature range of 25–200 ℃, indicating that there are less transferable charges in the sample and the insulation of the sample is good.

Comparing Fig. 2(a) with Fig. 2(b), we can see that: (1) Compared with the rapid cooling process, the slow cooling process significantly improves the dielectric constant of the sample, which is about 5600 for the SC sample at the T-C phase transition point, while about only 3600 for the RC sample. (2) The T-C phase transition of the SC sample is located at about 384 ℃, which is about 11 ℃ higher than that of the RC sample.

Figures 2(c) and 2(d) depict the room-temperature hysteresis loops of the two samples under different electric fields at 100 Hz. Both the samples exhibit standard ferroelectric hysteresis behavior, with the polarization and the coercive field E_c of the SC sample larger than those of the RC sample. As shown in Figs. 2(e) and 2(f), under 70 kV/cm, the maximum polarization P_m and the remanent polarization P_r of the SC sample are 32.6 μC/cm^2 and 13.5 μC/cm^2, respectively, while those of the RC sample are 24.3 μC/cm^2 and 7.7 μC/cm^2, respectively. The polarization (P_m, P_r) and the coercive field of the SC sample [Fig. 2(f)] increase nonlinearly with increasing applied field, showing a trend of saturation at larger field, while those of the RC sample [Fig. 2(e)] increase near linearly. These phenomena illustrate that, in addition to the better dielectric activity, the SC sample also possesses significantly enhanced ferroelectricity compared with the RC sample.

Based on the above results, we believe that the differences in dielectric and ferroelectric properties between RC and SC samples are dominated by the structural characteristics such as grain size, domain size, and lattice anisotropy, while not clearly correlated with the oxygen vacancy content. As we know, one of the possible effects of oxygen vacancies is causing a larger leakage current. However, the dielectric losses of the two samples are similar and both of them are quite low. Meanwhile, although the

SC sample possesses obviously more oxygen vacancies, its hysteresis loops do not show the characteristic arc-shaped end of leaky samples.[24] Another possible effect of the oxygen vacancies is pinning on polarization switching, leading to clamped hysteresis loops or increased coercive fields.[22] Nevertheless, the loops of the SC sample are normal and the coercive fields are close to that of the RC sample.

Now we try to explain the influence of structural characteristics on the dielectric and ferroelectric properties of the samples. In the SC sample, as the grain size increases and more hexahedral grains present, the degree of lattice anisotropy increases, leading to a larger intrinsic electric moment of each molecule and stronger interactions among them, and resulting in larger $P_{\rm m}$ and $P_{\rm r}$ under external electric field.[25] During the heating process of the dielectric measurement, a higher temperature is needed for the sample to eliminate the larger lattice anisotropy and transform into the cubic phase, meanwhile, the degrees of lattice anisotropy along with the phase transition point of different grains are close to each other, thus the dielectric peak corresponding to the T-C phase transition is higher and

appears at higher temperature [Fig. 2(b)]. On the contrary, in the RC sample, the lattice anisotropy, the intrinsic electric moment, and then the $P_{\rm m}$ and $P_{\rm r}$, are smaller. In addition, there are larger amounts of small grains that might be too small to be counted in the SEM image, as indicated by the broadened XRD peaks in Fig. 1(a), and the differences in the lattice anisotropy, intrinsic moment, and coercive voltage among grains with different sizes could be significant. Even more, due to the size effect, some of the small grains may turn to be paraelectric.[26] Thus, the electric hysteresis loops of the RC sample [Figs. 2(c) and 2(e)] show a linear trend compared to the SC sample [Fig. 2(d) and 2(f)]. During the heating process of dielectric measurement, a relatively lower temperature could be enough for the RC sample to eliminate the lattice anisotropy and transform to the cubic phase, meanwhile, the diverse lattice anisotropy leads to the dispersed phase transition point of different grains. As a result, the dielectric peak corresponding to the T-C phase transition of the RC sample is lower and appears at lower temperature.
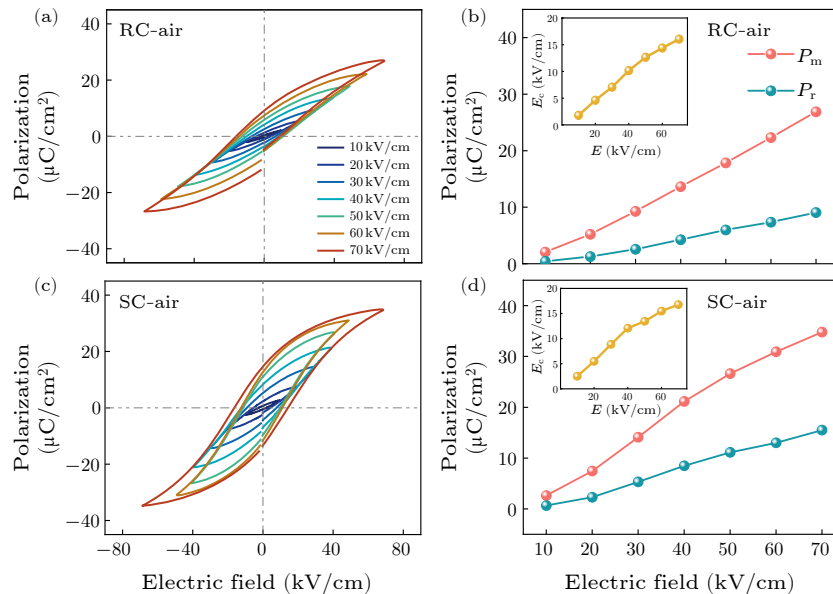
Fig. 3. [(a), (b)] Hysteresis loops of the RC and SC samples after 440 ℃ 30 min annealing in air (RC-air, SC-air). [(c), (d)] Parameter changes corresponding to (a) and (b).

Although we have emphasized the role of the structural features as mentioned above, oxygen vacancies also have undeniable impacts on the electrical properties of the samples. To illustrate this point, the samples were annealed at 440 ℃ for 30 min in air. For both the SC and RC samples after annealing (SC-air, RC-air), along with the increasing electric field, the $P_{\rm m}$ and $P_{\rm r}$ increase with a similar trend as those of the original samples, but the corresponding values become slightly larger, as shown in Fig. 3. This may be related to the decrease of oxygen vacancies in the annealed samples. As we know, oxygen vacancies could pin the polarization switching, the reduction of the oxygen vacancies would lead to an easier polarization switching.[22,27]

Since there are more oxygen vacancies in the SC sample, in order to clearly understand the impacts of oxygen vacancies, we conducted oxygenation treatment on the SC

sample, which was to raise the temperature to 440 ℃ in oxygen atmosphere and maintain for 30 min. The hysteresis loops and the corresponding parameter changes of the SC-O$_2$ sample are shown in Figs. 4(a) and 4(b). With a significant decrease in oxygen vacancy content [$I_{\rm O2}/I_{\rm O1}$ decreases to about 0.97 in Fig. 4(c)], the polarization of the SC-O$_2$ sample is evidently improved compared with that of the original SC [Figs. 2(d) and 2(f)] and the SC-air sample [Figs. 3(b) and 3(d)]. This result suggests that, in SC samples with better intrinsic structural integrity, it might be easier to modulate the sample performance by adjusting the oxygen vacancy content. To verify this, we further heat-treated (440 ℃, 30 min) the SC-O$_2$ samples in vacuum (deoxygenation). Figure 4(d) shows that, after vacuum heat treatment, the hysteresis loops of the SC-O$_2$ vacuum-annealed sample keep similar shapes with those

beforehand, indicating the robust ferroelectricity. However, the relevant parameters have changed, as shown in Fig. 4(e). The polarization (P_m, P_r) declines compared with that of the SC-O$_2$ sample, and is closer to the original SC sample. This should originate from the oxygen vacancies [I_{O2}/I_{O1} increasing to about 1.95 in Fig. 4(f)] and the

correspondingly enhanced pinning effects on polarization switching. The above series of results are depicted clearly in Fig. 5(a), demonstrating that the oxygen vacancy content can be modulated through heat treatment to achieve reversible control of ferroelectric polarization.
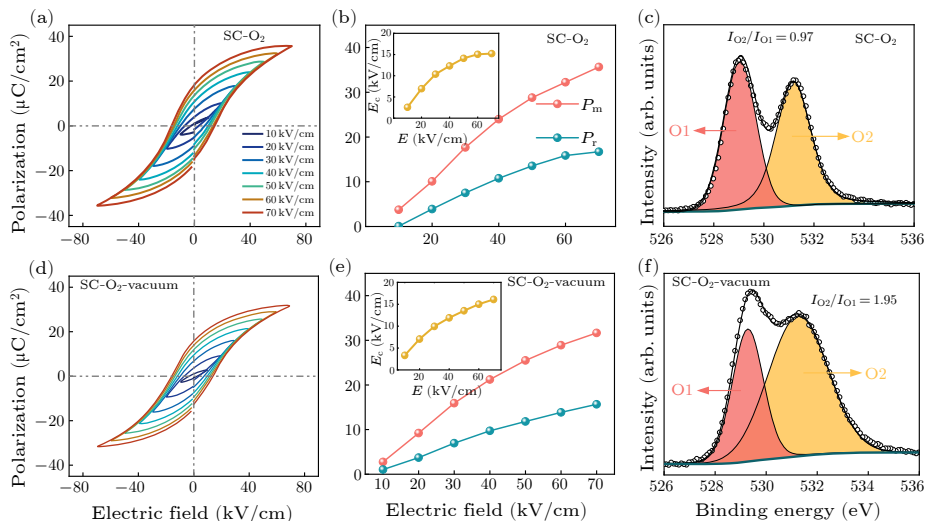
Fig. 4. Hysteresis loops (100 Hz), corresponding parameter changes, and XPS O 1s spectra of the SC samples [(a)–(c)] after 440 ℃ 30 min annealing in oxygen atmosphere (SC-O$_2$), and [(d)–(f)] after a subsequent vacuum annealing (SC-O$_2$ vacuum).
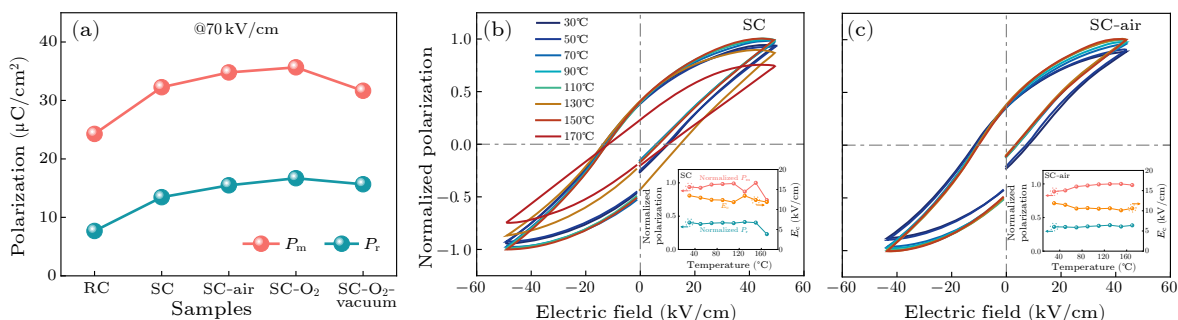
Fig. 5. (a) P_m and P_r of the samples after different thermal processing. Normalized hysteresis loops (50 kV/cm, 100 Hz) at different temperatures (b) for the as-grown SC sample and (c) for the SC sample after 440 ℃ 30 min annealing in air (SC-air). Insets depict the corresponding parameter changes with temperature.

For the application of ferroelectric materials, the temperature stability is one of the key points affecting the reliability of the devices. Figures 5(b) and 5(c) depict comparison of temperature stability of the hysteresis loops (50 kV/cm, 30–170 ℃) for the SC samples before and after annealing at 440 ℃ 30 min in air. To ensure that the sample is not electrically broken down during the high temperature measurement, the testing voltage we choose here is relatively small. In this case, the polarization of the samples does not reach the saturation state. Therefore, for a reasonable comparison, we normalize the P–E loops based on the maximum polarization in the measuring temperature range. It can be seen that after annealing, the variation of the hysteresis loops with temperature is obviously compressed. Taking P_m as an example, before annealing, the change of P_m within the measuring temperature range is about 21%, while after annealing, the change of P_m is significantly reduced to about 1.3%. Figure S4 shows the

temperature stability of the RC samples. Before and after annealing, the changes in P_m of the RC samples are approximately 1.17% and 1.03%, respectively. These results indicate the important role of the oxygen vacancy migration in the variation of ferroelectricity with temperature. Compared with the original SC sample, the content of oxygen vacancies in RC and the annealed SC samples are less, contributing to the better temperature stability of the electrical properties.

Researchers have reported on the effects of preparation conditions, especially the heating process and the maximum sintering temperature, on the structure and the properties of KNN. Due to the volatilization of K and Na elements, KNN is very sensitive to the preparation conditions, and usually has a narrow sintering window.[28,29] Different from literature, in this study we pay special attention to the influence of the cooling process after sintering. In order to clearly show this effect, we select

two cooling rates that are 20 times different and observe the significant changes caused to the samples. Here for the KNN-based ceramics, rapid cooling results in smaller grains/domains, and more linearized hysteresis loops closing to the energy storage requirements; while slow cooling tends to produce larger grains/domains, and rectangular hysteresis loops meeting the needs of information storage. In addition to the structural features, the commonly appeared oxygen vacancies in oxides also have an undeniable regulatory effect on material properties. In this work, the content of oxygen vacancies in the fine-grain RC sample is less than that in the large-grain SC sample, which is contrary to our usual understanding and could be attributed to the particularity of the way oxygen vacancies introduced. Here, for the KNN ceramics, where the commonly discussed charged defects are cation vacancies at A sites,[3,24] we introduce Ba^{2+} and Co^{2+} ions at A and B sites, to replace the original K^+/Na^+ and Nb^{5+} ions, respectively. Through this heterovalent doping, we consciously introduce oxygen vacancies. Since oxygen vacancies usually impact on the polarization switching through pinning and de-pinning processes, the atmosphere heat treatment could modulate the oxygen vacancy content, so as to control the ferroelectricity of the ceramics. Finally in this work, we have successfully introduced an appropriate amount of oxygen vacancies into large-grain SC samples with good lattice integrity, which not only ensures excellent ferroelectric properties, but also provides a certain degree of controllability.

In summary, we have synthesized potassium sodium niobate based ceramics $0.98(K_{0.5}Na_{0.5})NbO_3$-$0.02Ba(Nb_{0.5}Co_{0.5})O_{3-\delta}$ with heterovalent doping of Ba^{2+} and Co^{2+} ions at the A and B sites, respectively, using a solid-state reaction method. The samples sintered by two different cooling rates (slow cooling, SC; rapid cooling, RC) are both in orthorhombic phase at room temperature, with the SC sample possessing larger grains/domains and lattice anisotropy. The larger dielectric constant, Curie temperature, and ferroelectric polarization of the SC sample are mainly attributed to the larger inherent electric moment corresponding to the better lattice integrity. The oxygen vacancy content in SC samples can be reversibly regulated through heat treatment in different atmospheres, thereby obtaining robust and adjustable ferroelectric characteristics. This work demonstrates an effective method to regulate the properties of ferroelectric materials, that is, using heterovalent doping can introduce oxygen vacancies in ceramics with good structural integrity. This method is valuable for multi-field device applications of ferroelectric materials.

References

[1] Xing J, Huang Y, Xu Q, Wu B, Zhang Q, Tan Z, Chen Q, Wu J, and Zhu J 2021 *ACS Appl. Mater. Interfaces* **13** 28472

[2] Vats G, Bai Y, Zhang D, Juuti J, and Seidel J 2019 *Adv. Opt. Mater.* **7** 1800858

[3] Zhou M, Lu X, Xu X, Liu L, Lei L, Xiao S, Huang F, Wang X, and Zhu J 2018 *Ceram. Int.* **44** 14169

[4] Wu H, Lin Y B, Gong J J, Zhang F, Zeng M, Qin M H, Zhang Z, Ru Q, Liu Z W, Gao X S, and Liu J M 2013 *J. Phys. D* **46** 145001

[5] Kumar R and Singh S 2018 *Sci. Rep.* **8** 3186

[6] Balanov V A, Temerov F, Pankratov V, Cao W, and Bai Y 2023 *Solar RRL* **7** 2200995

[7] Sardana S, Saddi R, and Mahajan A 2023 *Appl. Phys. Lett.* **122** 162902

[8] Li R, Zhang G, Li Y, Zhao P, Sun Q, and Wang Y 2024 *Int. J. Appl. Ceram. Technol.* **21** 1170

[9] Saito Y, Takao H, Tani T, Nonoyama T, Takatori K, Homma T, Nagaya T, and Nakamura M 2004 *Nature* **432** 84

[10] Wang K and Li J F 2010 *Adv. Funct. Mater.* **20** 1924

[11] Zheng T, Yu Y, Lei H, Li F, Zhang S, Zhu J, and Wu J 2022 *Adv. Mater.* **34** 2109175

[12] Xiao D and Zhu J 2010 *Ferroelectrics* **404** 10

[13] Xu Z, Lou L Y, Zhao C L, Tang H C, Liu Y X, Li Z, Qi X M, Zhang B P, Li J F, Gong W, and Wang K 2020 *Acta Phys. Sin.* **69** 127705 (in Chinese)

[14] Ichangi A, Shvartsman V V, Lupascu D C, Lê K, Grosch M, Kathrin Schmidt-Verma A, Bohr C, Verma A, Fischer T, and Mathur S 2021 *J. Eur. Ceram. Soc.* **41** 7662

[15] Zhang N, Lv X, Zhang X X, Cui A, Hu Z, and Wu J 2021 *ACS Appl. Mater. Int.* **13** 60227

[16] Vats G, Peräntie J, Palosaari J, Juuti J, Seidel J, and Bai Y 2020 *ACS Appl. Electron Mater.* **2** 2829

[17] Wang Z C, Cui Z Z, Xu H, Zhai X F, and Lu Y L 2019 *Chin. Phys. B* **28** 087303

[18] Tang H, Tang X G, Jiang Y P, Liu Q X and Li W H 2019 *Acta Phys. Sin.* **68** 227701 (in Chinese)

[19] Shi W, Feng Y, Lu T, Lu Y, Shen J, Xue J, Du J, Fu P, Hao J, and Li W 2019 *J. Mater. Sci: Mater. Electron.* **30** 9

[20] Min K, Huang F, Jin Y, Lu X, Wu H, and Zhu J 2015 *J. Phys. D* **48** 445301

[21] Wu J, Xiao D, and Zhu J 2015 *Chem. Rev.* **115** 2559

[22] Lei L, Liu L, Lu X, Mei F, Shen H, Hu X, Yan S, Huang F, and Zhu J 2021 *ACS Appl. Mater. Int.* **13** 43787

[23] Tao H, Yin J, Zhao C, and Wu J 2021 *J Eur. Ceram Soc.* **41** 335

[24] Zhou M, Lu X, Liu L, Wang J, Lu D, Huang F, Zhu J, Cheng P, and Wang Q 2020 *J. Alloys Compd.* **836** 155519

[25] Yang Z, Gao F, Du H, Jin L, Yan L, Hu Q, Yu Y, Qu S, Wei X, Xu Z, and Wang Y J 2019 *Nano Energy* **58** 768

[26] Fong D D, Stephenson G B, Streiffer S K, Eastman J A, Auciello O, Fuoss P H, and Thompson C 2004 *Science* **304** 1650

[27] Lei L, Liu L, Lu X, Yan S, Hu X, He J, and Huang F 2023 *Adv. Opt. Mater.* **11** 2201893

[28] Du J, Wang J F, Zang G Z, and Yi X J 2011 *Chin. Phys. Lett.* **28** 067701

[29] Du J, Wang J F, Zheng L M, Wang C M, Qi P, and Zang G Z 2009 *Chin. Phys. Lett.* **26** 027701